Utah State University

DigitalCommons@USU

7-12-2019

Regional Distribution of Mesospheric Small-Scale Gravity Waves During DEEPWAVE

Pierre-Dominique Pautet
Utah State University, dmoiniquepautet@gmail.com

Michael J. Taylor
Utah State University, mike.taylor@usu.edu

S. D. Eckermann
U.S. Naval Research Laboratory

Neal R. Criddle
Utah State University, neal.criddle@aggiemail.usu.edu

Follow this and additional works at: https://digitalcommons.usu.edu/ail_pubs

Part of the Cosmology, Relativity, and Gravity Commons

Utah State University
MERRILL-CAZIER LIBRARY

Correspondence to:
P.-D. Pautet,
dominiquepautet@gmail.com

Regional Distribution of Mesospheric Small-Scale Gravity Waves During DEEPWAVE

P.-D. Pautet[1], M. J. Taylor[1], S. D. Eckermann[2], and N. Criddle[1]

[1]Center for Atmospheric and Space Sciences (CASS), Utah State University, Logan, UT, USA, [2]Space Science Division, U.S. Naval Research Laboratory, Washington, DC, USA

Abstract The Deep Propagating Gravity Wave Experiment project took place in June and July 2014 in New Zealand. Its overarching goal was to study gravity waves (GWs) as they propagate from the ground up to ~100 km, with a large number of ground-based, airborne, and satellite instruments, combined with numerical forecast models. A suite of three mesospheric airglow imagers operated onboard the NSF Gulfstream V (GV) aircraft during 25 nighttime flights, recording the GW activity at OH altitude over a large region (>7,000,000 km^2). Analysis of this data set reveals the distribution of the small-scale GW mean power and direction of propagation. GW activity occurred everywhere and during every flight, even over open oceans with no neighboring tropospheric sources. Over the mountainous regions (New Zealand, Tasmania, isolated islands), mean power reached high values (more than 100 times larger than over the waters), but with a considerable variability. This variability existed from day to day over the same region, but even during the same flight, depending on forcing strength and on the middle atmosphere conditions. Results reveal a strong correlation between tropospheric sources, satellite stratospheric measurements, and mesosphere lower thermosphere airglow observations. The large-amplitude GWs only account for a small amount of the total (~6%), even though they carry the most momentum and energy. The weaker wave activity measured over the oceans might originate from distance sources (polar vortex, weather fronts), implying that a ducted mechanism helped for their long range propagation.

1. Introduction

Short-period gravity waves (GWs) are mostly generated in the lower atmosphere and propagate horizontally and vertically, transporting energy and momentum to higher altitudes, and defining global circulation throughout the middle and upper atmosphere (e.g., Fritts & Alexander, 2003; Garcia & Solomon, 1985; Holton, 1983; Lindzen, 1981). In particular, they strongly affect the mean atmospheric structure (wind and temperature), the tides, and the planetary waves (e.g., Ribstein & Achatz, 2016 ; Yiğit & Medvedev, 2010). Numerous observation studies have been aimed at defining the characteristics of these waves and their effects on the mesosphere lower thermosphere (MLT), using ground-based instruments such as radars (e.g., Fritts et al., 2010; Reid & Vincent, 1987; Tsuda et al., 1990), lidars (e.g., Bossert et al., 2014; Collins et al., 1996, Gardner et al., 1995, Senft & Gardner, 1991, Williams et al., 2006), or imagers (e.g., Li et al., 2011; Medeiros et al., 2007 ; Moreels & Herse, 1977 ; Nakamura et al., 1999 ; Taylor et al., 1997). Each investigation focused on one observation site, and even if these sites are scattered worldwide, though mostly at low and middle latitudes, they only provide local information on GW characteristics. To extend the measurements over larger regions, aircraft, balloons, and satellites have been used, mostly for stratospheric studies, showing the distribution, intensity, and effects of GWs in the middle atmosphere (e.g., Alexander & Teitelbaum, 2011; Dewan et al., 1998; Eckermann & Preusse, 1999; Gardner, 1991, Gardner, 1995; Hertzog et al., 2012; Hoffmann et al., 2013; Jewtoukoff et al., 2013; Jiang et al., 2002; Wu & Waters, 1996). Only recently, satellite observations have revealed extensive mesospheric wave structures and their association with tropospheric forcing (Azeem et al., 2015; Miller et al., 2015; Perwitasari et al., 2016; Yue et al., 2014). However, the satellite borne instruments have a coarse resolution and a limited time sampling; thus, they fail to capture the smaller-scale GWs (horizontal wavelength < ~100 km). Recent theory and modeling indicate that those GWs have profound effects on the variability and mean state of the upper atmosphere system through divergences of GW momentum flux (MF) and energy flux (EF) (e.g., Eckermann et al., 2016; Fritts et al., 2014; Fritts & Alexander, 2003; Fritts & Lund, 2011; Yiğit & Medvedev, 2015), or transport and distribution of constituents (e.g., Gardner, 2018; Qian et al., 2009; Salinas et al., 2016), driving the weather and climate of the MLT. Global mesospheric GW measurements have also become more and

more necessary as global circulation models, which try to simulate the GW dynamics and effects up to MLT altitude or higher, cannot fully resolve the individual waves and therefore have to include parameterization schemes (e.g., Alexander & Barnet, 2007; Preusse et al., 2014). While computational power has dramatically improved in the past decade, GWs with horizontal wavelength below ~100 km cannot be directly simulated in global circulation models, although they carry a large part of the fluxes (Shutts & Vosper, 2011). Other GW characteristics are also not reproduced correctly like filtering, interactions, spectral evolution, or source intermittency (Geller et al., 2013).

Despite the importance of small-scale GWs in the Earth's atmosphere, many unknowns still exist. More quantitative large-scale (or even global) observations are necessary to fill this knowledge gap. For example, regional measurements can help answering questions about the effects of tropospheric forcing by comparing GW importance and effects in function of the distance from a source. The extent and spectrum of a GW field cannot be fully investigated from a single location, as well. Fully understanding of the importance of GW breaking and momentum deposition on the background atmosphere also requires regional-scale observations.

Large-scale measurements were achieved as part of the Deep Propagating Gravity Wave Experiment (DEEPWAVE) campaign, using an NSF aircraft, in June and July 2014. These measurements revealed the GW activity over a large region surrounding the New Zealand South Island (SI). A total of 26 research flights (RFs) were performed, covering a region extending from ~30°S to ~65°S in latitude, and from ~140°E to ~180°E in longitude (~7,000,000 km^2). The aircraft flew over both lands (New Zealand, Tasmania, sub-Antarctic islands), and oceans (Tasman Sea, Pacific Ocean, Southern Ocean), and during periods when different GW forcing and atmospheric conditions prevailed. The large amount of image data obtained during this project allows for measuring GW horizontal characteristics (wavelength, power, and direction of propagation) and comparing those with the environment (geographical location, GW forcing) at the time of the flight.

This study will investigate the small-scale GWs ($\lambda_h < 40$ km) obtained during the DEEPWAVE flights. Section 2 will give a short overview of the campaign, and describe the airglow imagers operated onboard the NSF aircraft. Section 3 will explain the analysis method used to extract the small-scale GW characteristics. Section 4 will discuss the GW variability, especially its relation with the location and evolution of the main GW sources. Finally, conclusions will be presented in section 5.

2. Instrumentation: Observations

2.1. The DEEPWAVE Campaign

Although knowledge on GWs has vastly improved in the past few decades, many questions remain, especially concerning their propagation throughout the middle and upper atmosphere and the effects of the atmospheric background on their life cycle (generation, propagation, and dissipation). To investigate these topics, a project named DEEPWAVE took place in June and July 2014 over New Zealand and its surroundings. This campaign was designed to better understand GW generation, propagation, and effects from their sources to their regions of dissipation (stratosphere or MLT), in function of the tropospheric forcing, the background atmosphere characteristics, and the GW parameters. A large suite of instruments was deployed at several ground-based sites, but also onboard two research aircrafts: an NSF Gulfstream V (GV) and a DLR Falcon. The GV aircraft was the centerpiece of the project. It performed 26 research flights between 6 June and 21 July. This period was at the beginning of the austral winter, when the middle atmosphere background conditions (eastward wind) allow deep GW propagation up to MLT altitude.

Instruments onboard the GV measured atmospheric parameters below the aircraft (dropsondes), at flight altitude (temperature, pressure, horizontal and vertical winds), and also remotely in the stratosphere (Rayleigh lidar), and in the MLT (Na lidar, Advanced Mesospheric Temperature Mapper or AMTM, infrared OH airglow imagers). The AMTM instrument suite is described in more detail below. In addition, the Atmospheric InfraRed Sounder instrument onboard the AQUA satellite (Aumann et al., 2003) provided near real-time temperature-sensitive radiances from ~20 to 42 km in the stratosphere, from which GW maps were derived. Finally, several high-resolution forecast models provided daily guidance in flight planning throughout the campaign. A more complete description of the DEEPWAVE project and several initial research
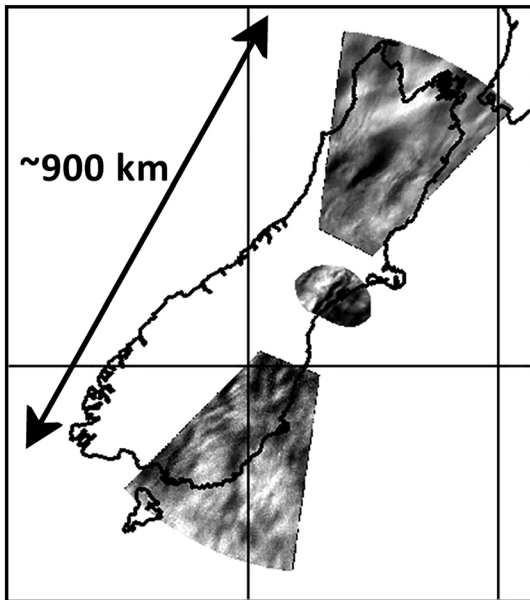
Figure 1. Projection on the map of the New Zealand South Island of the fields of view of the three airglow imagers operated onboard the GV aircraft during DEEPWAVE.
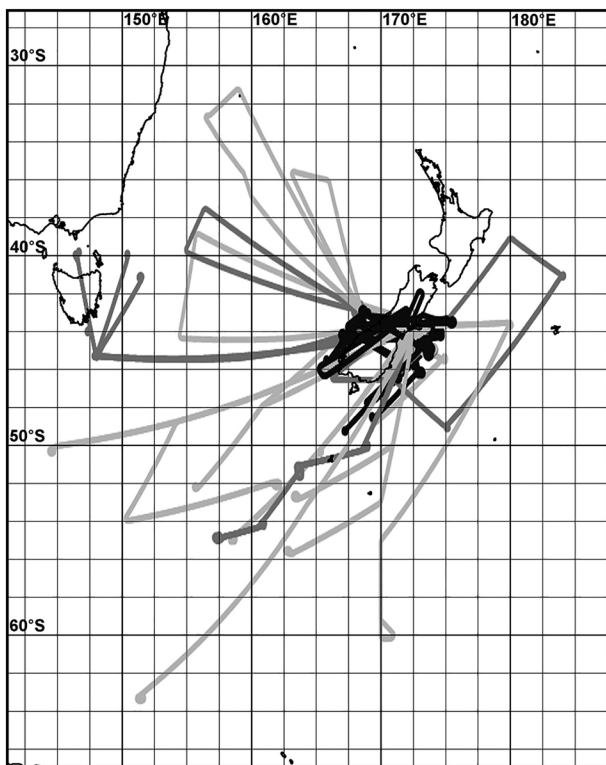
highlights are given by Fritts et al. (2016). Other DEEPWAVE studies addressing various GW dynamics and involving AMTM observations include Bossert et al. (2015, 2017), Bramberger et al. (2017), Eckermann et al. (2016), Fritts et al. (2018), Heale et al. (2017), Pautet et al. (2016), and Portele et al. (2018).
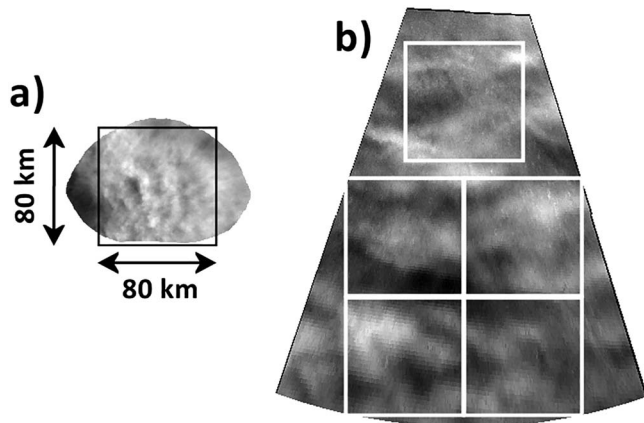
2.2. Advanced Mesospheric Temperature Mapper Instrument Suite

The GV AMTM measures the atmospheric temperature over an ~120 × 80-km region centered near zenith, using the OH (3,1) band emission. This bright emission originates from an ~7–8-km-thick layer located at ~87 km, and is widely used since the early 1970s as a tracer of the dynamical processes in the MLT (e.g., Li et al., 2011; Medeiros et al., 2007; Moreels & Herse, 1977; Nakamura et al., 1999; Taylor et al., 1997). The AMTM was designed and built at Utah State University. It uses a 320 × 256-pixel infrared sensor and a computer-controlled filter wheel to sequentially measure the brightness of the $P_1(2)$ and $P_1(4)$ lines of the OH (3,1) band, as well as the atmospheric background. Combining these three emissions, it is possible to process the OH (3,1) rotational temperature for each pixel of an image and "map" the mesospheric temperature over a large region. More details about this instrument are given in Pautet et al. (2014). For DEEPWAVE, the AMTM was slightly modified: its field of view was ~80 × 60° (instead of 120° circular), with the longest dimension parallel to the direction of motion of the aircraft. The exposure time for each filter was typically 4 s, providing a temperature and an intensity maps every 16–17 s (because of the short extra time needed to save each image and to rotate the filter wheel). In addition to the AMTM, two low-elevation (field of view centered at 25° elevation angle) infrared imagers were installed on each side of the plane. They measured only the OH emission brightness, but their wide field of view (~40° horizontal × 30° vertical, which corresponds to an approximately trapezoidal region with a 330-km large base located 450 km away from the aircraft at OH layer altitude) provided the larger-scale context for the vertically viewing lidar and AMTM measurements in the MLT. These cameras' sensitivity extend from 900 to 1,600 nm, allowing for short exposure times (3–4 s), and a higher cadence than the full AMTM sequence (16–17 s). As an example of the data obtained during DEEPWAVE, Figure 1 shows three OH airglow intensity images taken simultaneously by the AMTM and the two side cameras during research flight 12 (RF12), and projected onto a map of the New Zealand (NZ) SI. The projections do not overlap but they still cover a large region (~900 km) and exhibit structures typical of GW activity.

2.3. The DEEPWAVE Research Flights

The GV long-range capability (~9,000 km), cruising altitude (~12 km) and instrument suite, allowed to sample many regions of interest, depending on the forecasted GW sources (orography, convection, frontal system, or jet stream) and propagation environment. A total of 26 GV RFs were conducted during the DEEPWAVE campaign. Twenty five of them were performed during nighttime, when the imagers were able to make airglow measurements. Figure 2 shows the flight paths for these 25 flights. A large number of them were dedicated to mountain wave observations over the NZ SI (RFs 04, 05, 08, 10, 12, 13, 14, 16, 21, 22, and 26), some focused on mostly oceanic regions (RFs 01, 03, 11, 17, 18, 19, 20, 24, and 25), while

Figure 2. Flight paths of the 25 nighttime DEEPWAVE research flights. Black corresponds to mountain wave focused flights, light grey to open ocean flights, and dark grey to a combination of both.

Figure 3. (a) Projection of the zenith imager field of view and the 80 × 80-km box selected for the FFT analysis. (b) Similar representation but for one of the side-viewing imagers. This time, the larger field of view allows for the FFT to be processed on the five 80 × 80-km white boxes.

some combined the two types of environment (RFs 02, 06, 07, 09, and 23). As seen in Figure 2, the coverage was extensive and the entire region surrounding NZ was sampled at some point in the campaign (the black flight paths correspond to RFs focused on mountain wave activity, light grey to open ocean flights, and dark grey to a combination of both). Such coverage allows for investigating the small-scale GW characteristics depending on the source regions or the tropospheric forcing not only from night to night but also during a single flight. To the extent of our knowledge, previous ground-based airglow measurements never permitted similar investigation.

3. Data Analysis: Results

3.1. Data Analysis

This study involves not only images taken by the AMTM but also by the side cameras. As shown in Figure 1, the shape of the projected pictures is irregular; therefore, square regions have to be selected from each image to properly 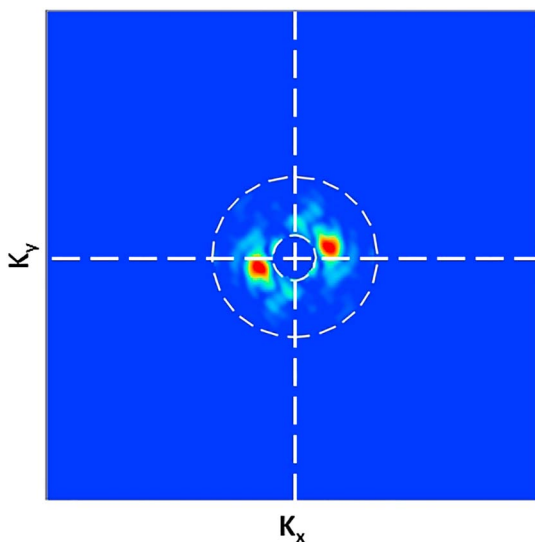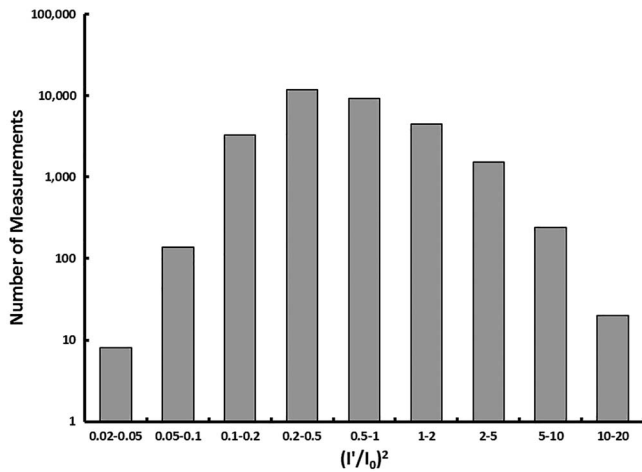apply an FFT analysis process. Figure 3a shows an 80 × 80-km square superimposed on an AMTM intensity image. The side camera projection on Figure 3b is larger, so in this case, to do a similar analysis, five 80 × 80-km squares have been drawn. Each of these small regions is isolated and a 2-D fast Fourier transform (FFT) algorithm is applied to it. This processing converting the spatial image data into frequency space is typical for airglow image analysis and has been used in many previous investigations (Coble et al., 1997; Garcia et al., 1998). Nevertheless, this time, just part of the resulting spectrum is taken into account. The power spectrum corresponding to the region of interest in Figure 3a is shown in Figure 4, but only the region between the two white dashed circles is relevant to this analysis. It corresponds to horizontal wavelengths between 10 (large circle) and 40 km (small circle). Numerous short-period GW studies have shown that wavelengths smaller than 10 km are associated with nonpropagating localized turbulent events, the so-called "ripples" (e.g., Hecht et al., 1997), while most of the other short-period GWs have horizontal wavelengths less than ~40 km. For example, Medeiros et al. (2003), using all-sky OH images obtained from a low-latitude site in Brazil, measured 179 events. They showed that ~90% of them had a horizontal wavelength <40 km. Nielsen et al. (2006), using the same type of instrument, but this time from Halley, Antarctica (76°S), measured 221 events during two austral winters. Again, ~90% of the waves had horizontal wavelengths <40 km. In their paper, they list other studies that obtained very similar results from middle- and low-latitude locations. These small-scale GWs are indeed of great interest as they carry a large part of the momentum affecting the upper atmosphere (Fritts et al., 2014; Fritts & Alexander, 2003). Limiting the analysis to these waves, even if also dictated by the field of view of the instruments, is still relevant and can provide a major insight on the GWs propagating at MLT altitude.

Spectra have been calculated for all the intensity images taken by the AMTM (one spectrum) and the two side cameras (five spectra each). The periods of observation just after takeoff, soon before landing, and each time the GV turned, were excluded from the analysis.

Two parameters have been extracted from the spectra: the average power for the 10–40-km GWs (obtained by integrating all the values between the two circles and between 0° and 180° azimuth) and the main direction corresponding to this power, Θ (calculated by integrating the power along each radius, every degree, for 10 km < λ_h < 40 km, and then selecting the largest broad peak). Θ values range only between 0° (north) and 180° (south), as the 2-D FFT analysis creates a 180° ambiguity. Finally, the results have been geographically binned into 2.5° (in longitude) × 2° (in latitude) regions, which correspond to ~160 × 220-km areas at 45°S.

Figure 4. Typical power spectrum for one of the 80 × 80-km boxes. Only the power corresponding to the GWs with horizontal wavelengths between 10 km (larger circle) and 40 km (smaller circle) is taken into account. Note the 180° ambiguity due to the FFT algorithm.

Figure 5. Number of measurements versus $(I'/I_0)^2$ for the 25 nighttime research flights.

Any region with less than 20 measurements (one measurement corresponding to a set of values power + direction; there are five measurements for each side image, and one measurement for each zenith image) has been ignored before analyzing the results.
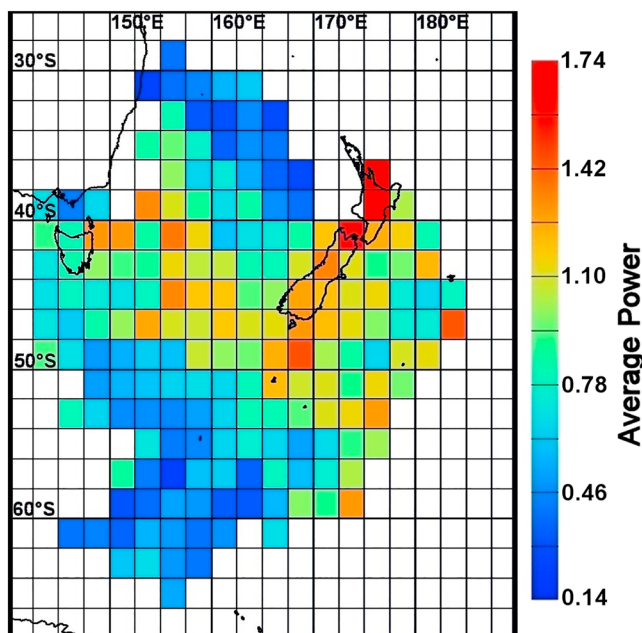
3.2. Results

More than 30,000 80 × 80-km regions have been analyzed. Figure 5 shows how the results are distributed in function of the relative intensity perturbation power $(I'/I_0)^2$ (with I_0 corresponding to the average intensity for the selected region in an image). $(I'/I_0)^2$ varies from 0.03, when almost no waves were present, to 14.6, during large-amplitude mountain wave (MW) events. Note that each $(I'/I_0)^2$ value reflects the average power for an 80 × 80-km region, and for 10 km $< \lambda_h <$ 40 km, not for a single GW event. Ninety-four percent of the measurements correspond to 0.1 $< (I'/I_0)^2 <$ 2. The largest values ($(I'/I_0)^2 >$ 2, ~100 times the minimum measurements) are relatively rare (~6%), even though they are associated with waves transporting very large amounts of momentum flux, which is proportional to $(I'/I_0)^2$. Similar results have been found by Cao and Liu (2016) who have analyzed OH airglow data obtained from Maui, HI (20.7°N) and Cerro Pachon, Chile (30.3°S).

To understand the geographical distribution of the measured GWs, the data plotted in Figure 5 have been binned into 2.5° (in longitude) × 2° (in latitude) regions, as shown in Figure 6. The extrema, this time, are 0.14 and 1.73. This range is narrower than for Figure 5, as these values correspond to the means of all the measurements inside a 2.5° × 2° region (from a few tens up to ~10,000). Similar analysis has been performed on the zenith temperature images (not shown). The results were similar to the intensity plot but with a much smaller number of values and a smaller coverage; therefore, the rest of the investigation was done using intensity measurements.

The first result is that the smallest average (0.14, ~8% of the largest value) shows that some GW activity was always present. It is important to notice that some areas have a much larger number of measurements (up to ~10,000), especially over NZ, while others have only a few tens, like the region far south. Nevertheless, the distribution is revealing: regions with larger power correspond to New Zealand, the ocean south of the South Island, and the south-east of Tasmania. The open ocean (north of the Tasman Sea, the Antarctic Southern Ocean, and in a lesser extent the Pacific Ocean east of NZ) exhibits lesser GW activity. Such unique result seems to reinforce the idea that the tropospheric forcing (convection, orography) directly affects the MLT above or close to it. To further investigate the differences between these two types of region Figure 7 shows the directionality associated with the average power in each geographical bin. It is important to keep in mind that each line indicates the average wave vector, not the waves themselves, and also that, due to the 2-D FFT processing, a 180° ambiguity exists on the direction of propagation. Once more, there are two different regimes which seem to be correlated with the GW power: over NZ and slightly to the south, over Tasmania, and over the Tasman Sea, the GWs propagated eastward (or westward), while over the open ocean, they had a tendency to propagate toward the northeast (or southwest).

4. Discussion

The GW power and directionality have been measured for the 25 DEEPWAVE nighttime flights using OH airglow image data, and mapped to reveal their geographical distribution over the NZ surroundings. This

Figure 6. Average power of the small-scale GWs (10 km $< \lambda_h <$ 40 km) observed during the 25 nighttime DEEPWAVE flights, and binned into 2.5° × 2° regions.
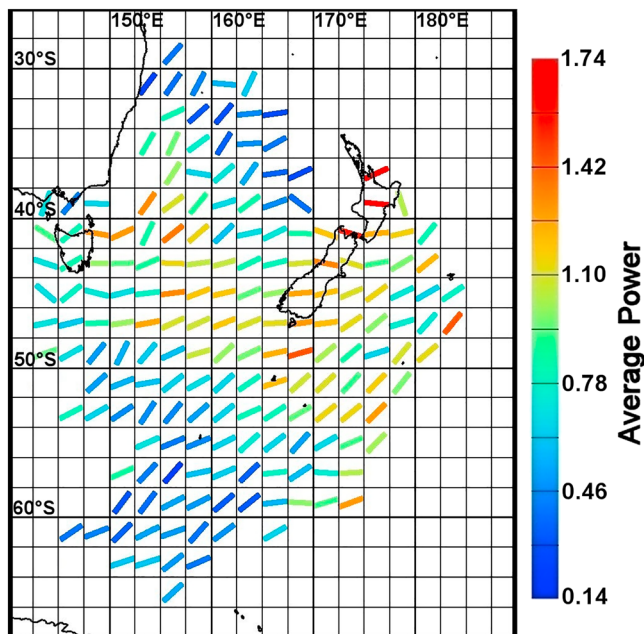
Figure 7. Same as Figure 5 but the average direction in each region is represented by a line giving the average wave vector. Note the 180° ambiguity.
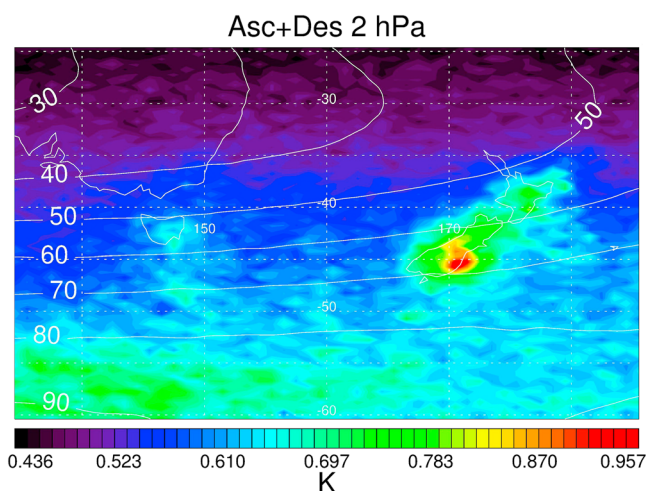
distribution shows two main regions depending if the measurements were obtained over/close to lands, or over open waters.

Atmospheric conditions during DEEPWAVE have been investigated in detail by Gisinger et al. (2017). They found out that during the June–July 2014 period, the main GW forcing was due to the displacement of the subtropical or the polar front jets, especially over the NZ SI, resulting in the generation of orographic waves. The stratospheric planetary wave activity also increased during the second part of the campaign, displacing the Antarctic polar vortex, and limiting the deep propagation of large-amplitude waves. The main tropospheric sources were therefore associated with mountainous regions, mostly NZ, Tasmania, and some small islands.

Figure 8 presents the root-mean-square perturbation brightness-temperature amplitudes for June–July 2014, due to stratospheric gravity waves, resolved in 15-μm radiances acquired by Atmospheric InfraRed Sounder channel 74 (wave number 667.53 cm^{-1}), which peaks near 2 hPa. Contours show corresponding mean reanalyzed horizontal wind speeds (m/s) at this nominal 2-hPa pressure level from the DEEPWAVE reanalysis of Eckermann et al. (2018). The covered region ranges from 25°S to 60°S, and from 134°E to 176°E, encompassing most of the DEEPWAVE airglow observations. The geographical distribution is strikingly similar to the mesospheric map of Figure 6. The largest values appear over NZ. Tasmania and the small islands south of NZ (e.g., Stewart and Auckland Islands) also show moderate GW activity. There seems to be a general connection between the sources in the troposphere, the satellite stratospheric measurements, and the mesospheric airglow observations. It might not be a direct connection, though: a large number of GWs generated in the lower atmosphere could have propagated up to the stratosphere and even managed to reach the mesosphere, but they might also have broken and generated secondary waves which were observed at higher altitude.

Results from individual nights are not so straightforward. In fact, there was a strong variability, especially over the NZ SI, where most flights were performed. To illustrate this result, Figure 9 shows the standard deviation for the mean $(I'/I_0)^2$ plotted in Figure 6. The color in each 2.5° × 2° bin represents the GW power variability in that small area. The smallest standard deviation was 0.03 (blue, most of the measurements close to the average value), and the largest 0.64 (red, large fluctuations). Of course, the regions with fewer observations (one or two RFs), close to the edges of the studied area, generally do not have a large variability. Nevertheless, it is interesting to notice that the largest variability appears to be associated with the mountain wave flights over NZ. The region of the Tasman Sea shows moderate variability, with a nonnegligible number of RFs (4–6), while the ocean further south has less variability with about the same number of measurements.

The most interesting cases occurred when the GV flew over two of these regions during the same night; the difference appears even more clearly. For example, Figure 10 shows the directionality and power for RF07 (a), RF11 (b), and RF25 (c). During RF07, even if the power was still moderate, the directionality changed off the east coast of NZ. RF11 exhibits substantial differences in both power and direction as the GV flew over the Tasman Sea. For RF25, the directionality remained mostly similar, but the GW power has dropped significantly over the Southern Ocean. The orientation can be explained by the difference in the GW sources. AMTM observations obtained during DEEPWAVE exhibited numerous N-S aligned standing waves, which were identified as mountain waves

Figure 8. Root-mean-square perturbation brightness-temperature amplitudes for June–July 2014, acquired by AIRS channel 74, near 2 hPa. Contours, with values ranging from 30 to 90 m/s, show corresponding mean reanalyzed horizontal wind speeds (m/s) at this nominal 2-hPa pressure level.
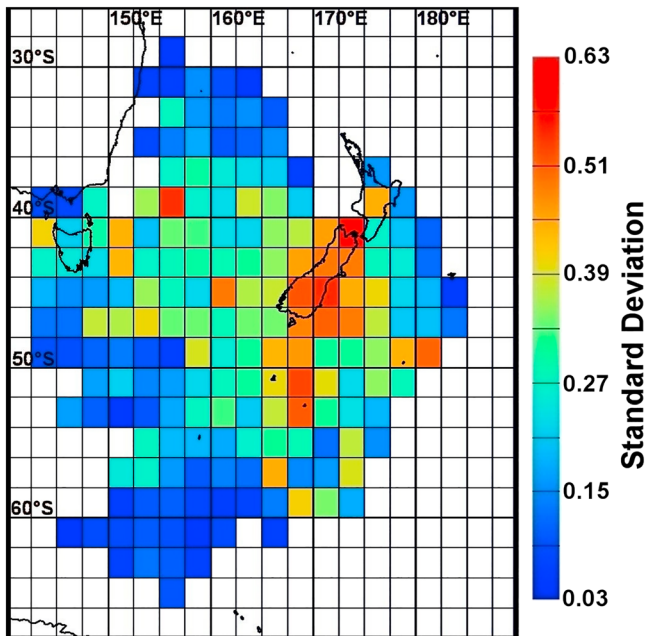
Figure 9. Same as Figure 5 but for the standard deviation of the small-scale GW power in each 2.5° × 2° regions.

(e.g., Bossert et al., 2015; Bramberger et al., 2017). Furthermore, this correlation between the sources and the GWs observed in the middle and upper atmosphere has been already noticed. Previous studies have investigated GW intermittency (the variation in the GW occurrence during a short period of time and over a limited area), mostly using momentum flux, over different regions. Long-duration stratospheric balloon measurements over the Antarctic continent have shown that orographic waves have larger amplitude but are more localized and sporadic than nonorographic ones (Hertzog et al., 2008; Plougonven et al., 2013). Similar results have been found worldwide using global satellite data (Wright et al., 2013). More recently, Cao and Liu (2016) have analyzed airglow images from two very distinct locations: an isolated ocean site, Maui, HI (20.7°N), and Cerro Pachon (30.3°S), in the Chilean Andes Mountains. They found that, at mesospheric altitude, intermittency is larger over the ocean site, in contrast with stratospheric observations. They attributed this to the fact that atmospheric background becomes more and more prominent compared to the GW source characteristics when reaching higher altitudes.

The GV airglow observations do not allow to precisely measure the GW phase speeds, which are necessary to estimate the momentum flux, because of the short duration each wave was visible (<8 min). Nevertheless, $(I'/I_0)^2$ is a good proxy for momentum flux, which is directly proportional to the relative wave perturbation squared (Fritts et al., 2014; Gardner et al., 1999). During DEEPWAVE, small-scale GW power was clearly associated with the tropospheric sources, especially the mountainous regions in NZ and Tasmania (see Figures 6 and 8), but differences also existed over a same region from flight to flight as revealed by Figure 9. The largest variability appeared over the South Island, where lots of flights focusing on mountain wave activity were performed. Normally, it was decided to fly when the forecast was most promising: in the case of orographically generated waves, when the tropospheric wind flowing on the mountain range was strong and when the assumed conditions in the middle atmosphere allowed for deep vertical propagation. Nevertheless, measurements at mesospheric altitudes did not always exhibit mountain wave activity. For example, Figures 11a and 11b show low GW power over NZ for two flights (RF05 and RF26, respectively). The binning in this case is 1° × 1° (~80 × 100 km at 45°S) because of the large number of measurements and the smaller region covered by the flights. Even though the forcing was deemed sufficient, the power is very small, indicating weak small-scale GW activity in the MLT. Similar cases occurred for RF04 and RF21. In contrast, Figures 11c and 11d present examples of large GW power, as was expected
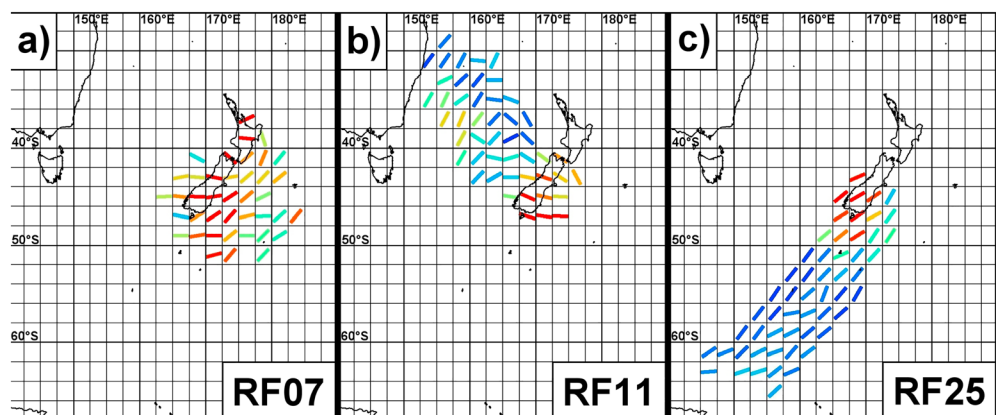
Figure 10. Same as Figure 6 but for individual RFs: (a) RF07, (b) RF11, and (c) RF25. The power and direction of the GWs vary strongly, depending if the GV was flying over lands or over oceans.
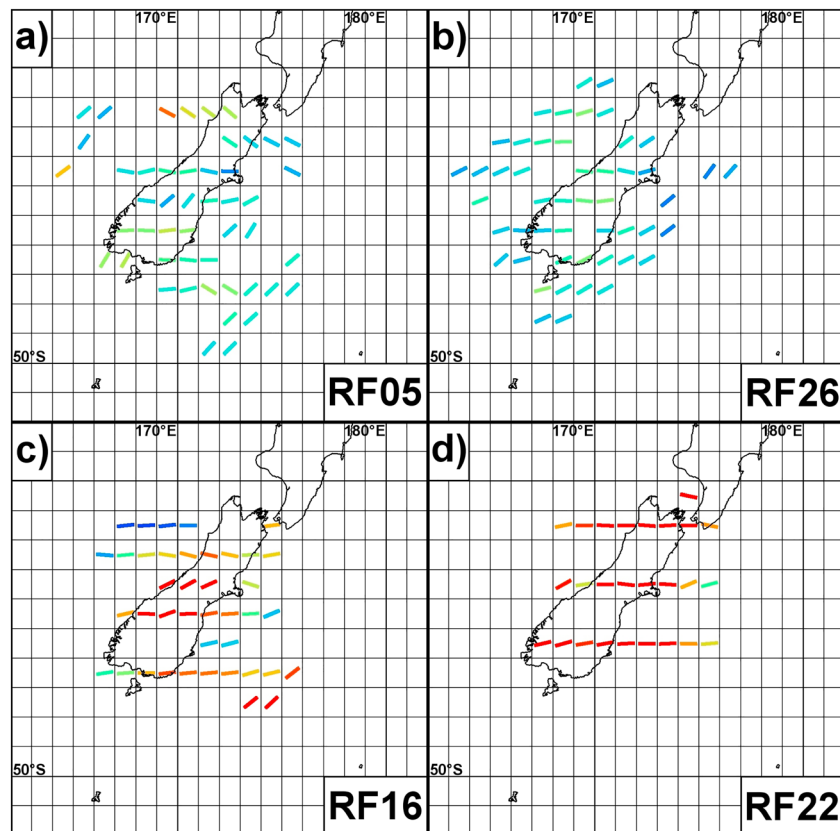
Figure 11. Same as Figure 6 but for mountain wave-focused research flights: (a) RF05, (b) RF26, (c) RF16, and (d) RF22. The dimensions of the binning regions are 1° × 1°. Note the difference in GW power and direction between RFs 05 and 26, and RFs 16 and 22, even if they were performed over the same region.

by the forecasts (RF16 and RF22, respectively). RF08, RF10, RF12, RF13, and RF14 exhibited comparable results. The directionality seems also correlated with the GW power: Figures 11c and 11d show perfect west-east direction of propagation while Figures 11a and 11b are not so homogeneous, with many bins indicating SW-NE directions.

In fact, the GW activity, especially when associated with orographic forcing, is complex in this region. Kaifler et al. (2015) have analyzed Rayleigh lidar data obtained from Lauder, NZ (45°S), from mid-June to November 2014, covering most of the DEEPWAVE campaign. They have investigated the case of mountain waves generated over the Southern Alps, showing that two main factors affected their propagation into the middle and upper atmosphere. The first one is the tropospheric wind forcing, which, if generating large-amplitude waves, increases the possibility of wave breaking at low altitude. The second factor is the wind minima around 15–25 km, or so-called "valve layer" (Kruse et al., 2016), which attenuates the amplitude of these MW events and filters part of the wave spectrum, thus allowing them to propagate to higher altitude. In a case study focusing on RF16, Bramberger et al. (2017) have discovered that a third element can affect the MW propagation into the mesosphere: the Polar Night Jet (50–60 km), if located over the NZ mountains, can partially reflect the waves, or even trap them around stratopause altitude. These recent results show the complexity of GW propagation over a mountainous region, and can explain the variability of the wave power and direction measured during the research flights.

As shown in these papers, the important small-scale GW activity observed during the DEEPWAVE research flights over the NZ SI is strongly related to orographic forcing in the troposphere. Of course, not all the MWs were able to reach the MLT as some broke at lower altitude. Nevertheless, secondary gravity waves were generated in the stratosphere or in the lower mesosphere and also propagated up to the OH layer altitude, where they were measured by the Utah State University imagers. Such cases have been described by Bossert et al.

Figure 12. Mapping of the OH brightness measured with the three GV imagers during the last leg of RF26. An extensive monochromatic small-scale GW field covers the whole region.

(2017), using Rayleigh and Na lidar data obtained onboard the GV during RF12 and 22, and by Heale et al. (2017), who simulated the partial breaking of a large MW event around 70-km altitude, thus revealing the origin of the small-scale waves observed in the MLT by the lidar and imagers during RF22 (Bossert et al., 2015).

Orographic forcing affecting the MLT does not always come from large mountain ranges. For example, the peak of power observed just south of NZ (around 50°S) in Figures 6 and 7 is due to the Auckland Islands archipelago. Strong MW activity has been measured in this area during RF23, even far from large mountains (Pautet et al., 2016). Eckermann et al. (2016) have modeled these waves and confirmed their orographic origin and showed that had a large impact on the MLT, as their momentum flux reached a value >300 m^2/s^2. Recent studies involving stratospheric measurements and modeling have revealed the unexpected effects of the Southern Ocean small isolated islands on the middle atmosphere (e.g., Wu et al., 2006; Alexander et al., 2009; Vosper, 2015). DEEPWAVE observations suggest that orographic waves generated over those islands might also strongly affect the MLT.

Waves associated with orographic forcing constituted the main part of the small-scale GW power during DEEPWAVE, but Figure 7 exposes a second GW regime, with smaller power and a slightly different direction of propagation (SW-NE instead W-E). This wave activity seemed to be ever present during all the DEEPWAVE flights. The corresponding wavefield extended from the region far south (~65°S), over the open ocean, up to ~30°S, close to Australia, and was visible over NZ or Tasmania when no strong orographic waves reached the MLT (see Figures 11a and 11b). Such general propagation direction has been reported before from many midlatitude airglow observation sites, and defined as "toward the summer pole" (see Nielsen et al., 2009, Table 1; Walterscheid et al., 1999), with usually a small zonal component. There have been many suggestions in previous studies concerning the origin of these GWs, most of them being related to local sources (convection, mountains, or weather fronts). The DEEPWAVE airglow data show that these waves have a very large extent (up to several thousand kilometers), and thus do not originate from any neighboring localized sources, which open up to another possibility: ducted waves coming from a faraway region. Indeed, ducting allows for GWs to propagate over long distances (e.g., Heale et al., 2014; Pautet et al., 2005, 2018). The ducted waves exhibit distinct observable characteristics (short ground-relative periods and high phase velocities), and they tend to be quasi-monochromatic and coherent (e.g., Snively & Pasko, 2005, and references therein). As an example, Figure 12 shows the airglow intensity mapping, made with the three GV imagers, corresponding to one of the legs performed over the NZ SI during RF26. Monochromatic small-scale waves are visible even far from the land, and the wavefield covered the entire observable area during the whole flight. It did not seem to be correlated with local sources and have characteristics typical of ducted waves. Possible sources for those GWs would be the displacement of the polar vortex or tropospheric frontal systems close to Antarctica. In both cases, the waves would have to have propagated several thousands of kilometers, which implies that they would have been ducted at some point. More detailed investigation of this case and other similar ones using atmospheric background data (e.g., NAVGEM reanalysis model) may show the nature of the GW propagation, but this study would be beyond the scope of this paper.

5. Conclusion

Small-scale mesospheric GWs have been measured using three airglow imagers during 25 RFs performed as part of the DEEPWAVE project. The observed region covered a large area (>7,000,000 km^2) including NZ and its surroundings, providing information on the GW activity at OH layer altitude over different sources during a two-month period, encompassing a large variety of forcing and background atmosphere

conditions. The small-scale GW average power and direction have been calculated, and the results mapped to determine their distribution and the possible connection between the GW sources, the propagation conditions, and their observation at MLT altitude. The main results are as follows:

- There is always some weak GW activity over every regions, with smaller GW power over the open waters (~10% of the largest mean power measured over NZ), especially the Southern Ocean.
- The very large $(I'/I_0)^2$ values (more than 100 times the smallest ones) account only for ~6% of the total measurements, even if they correspond to the waves transporting the most momentum.
- Seventy percent of the $(I'/I_0)^2$ values are below the average value (0.76).
- Larger power corresponds to landmasses, especially over higher-altitude regions, but even small isolated islands can have an unexpected impact at MLT height (Eckermann et al., 2016).
- Directionality follows the same pattern, with eastward (westward) propagation over the regions with strong tropospheric forcing (possibly associated with orographic sources), while northeastward (southwestward) propagation prevails over the other regions.
- The small-scale GW power at mesospheric altitude is, generally, directly associated with the tropospheric region under it, and correlates well with stratospheric satellite measurements.
- There is a large variability over the mountainous areas, depending on the strength of the orographic forcing, but also on the propagation conditions in the middle atmosphere. The extended small-scale wavefield covering the whole region surrounding NZ might correspond to ducted waves coming from a source possibly thousand kilometers further south, such as the polar vortex.

In summary, the small-scale GW activity at MLT altitude seems to be driven by two factors: the tropospheric sources intensity and duration, and the background environment (horizontal wind, vertical temperature profile) between the GW sources and the upper atmosphere. A strong correlation exists between tropospheric sources, stratospheric measurements, and airglow observations, indicating that, when conditions are favorable, GW generated in the lower atmosphere can propagate up to MLT altitude (being through primary or secondary GWs), where they may have direct and sometimes strong effects on the MLT (e.g., Eckermann et al., 2016; Pautet et al., 2016). When these waves cannot reach the MLT altitude, weak GWs are still measured everywhere, coming from the south west in the DEEPWAVE case.

Further case by case investigations using the results presented in this paper should be performed to have a better understanding of the conditions necessary to deep gravity wave propagation.

References

Alexander, M. J., & Barnet, C. (2007). Using satellite observations to constrain gravity wave parameterizations for global models. *Journal of the Atmospheric Sciences*, *64*(5), 1652–1665. https://doi.org/10.1175/JAS3897.1

Alexander, M. J., Eckermann, S. D., Broutman, D., & Ma, J. (2009). Momentum flux estimates for South Georgia Island mountain waves in the stratosphere observed via satellite. *Geophysical Research Letters*, *36*, L12816. https://doi.org/10.1029/2009GL038587

Alexander, M. J., & Teitelbaum, H. (2011). Three-dimensional properties of Andes mountain waves observed by satellite: A case study. *Journal of Geophysical Research*, *116*, D23110. https://doi.org/10.1029/2011JD016151

Aumann, H. H., Chahine, M. T., Gautier, C., Goldberg, M. D., Kalnay, E., McMillin, L. M., et al. (2003). AIRS/AMSU/HSB on the Aqua mission: Design, science objectives, data products, and processing systems. *IEEE Transactions on Geoscience and Remote Sensing*, *41*(2), 253–264. https://doi.org/10.1109/TGRS.2002.808356

Azeem, I., Yue, J., Hoffmann, L., Miller, S. D., Straka, W. C. III, & Crowley, G. (2015). Multisensor profiling of a concentric gravity wave event propagating from the troposphere to the ionosphere. *Geophysical Research Letters*, *42*, 7874–7880. https://doi.org/10.1002/2015GL065903

Bossert, K., Fritts, D. C., Kruse, C. G., Williams, B. P., Heale, C. J., Pautet, P.-D., et al. (2017). Secondary gravity wave generation over New Zealand during the DEEPWAVE campaign. *Journal of Geophysical Research: Atmospheres*, *122*, 7834–7850. https://doi.org/10.1002/2016JD026079

Bossert, K., Fritts, D. C., Pautet, P.-D., Taylor, M. J., Williams, B. P., & Pendleton, W. R. (2014). Investigation of a mesospheric gravity wave ducting event using coordinated sodium lidar and Mesospheric Temperature Mapper measurements at ALOMAR, Norway (69°N). *Journal of Geophysical Research: Atmospheres*, *119*, 9765–9778. https://doi.org/10.1002/2014JD021460

Bossert, K., Fritts, D. C., Pautet, P.-D., Williams, B. P., Taylor, M. J., Kaifler, B., et al. (2015). Momentum flux estimates accompanying multi-scale gravity waves over Mt. Cook, New Zealand on 13 July 2014 during the DEEPWAVE campaign. *Journal of Geophysical Research: Atmospheres*, *120*, 9323–9337. https://doi.org/10.1002/2015JD023197

Bramberger, M., Dörnbrack, A., Bossert, K., Ehard, B., Fritts, D. C., Kaifler, B., et al. (2017). Does strong tropospheric forcing cause large-amplitude mesospheric gravity waves? A DEEPWAVE case study. *Journal of Geophysical Research: Atmospheres*, *122*, 11,422–11,443. https://doi.org/10.1002/2017JD027371

Cao, B., & Liu, A. Z. (2016). Intermittency of gravity wave momentum flux in the mesopause region observed with an all-sky airglow imager. *Journal of Geophysical Research: Atmospheres*, *121*, 650–663. https://doi.org/10.1002/2015JD023802

Coble, M. R., Papen, G. C., & Gardner, C. S. (1997). Computing two-dimensional unambiguous horizontal wavenumber spectra from OH airglow images. *IEEE Transactions on Geoscience and Remote Sensing*, *36*(2).

Collins, R. L., Tao, X., & Gardener, C. S. (1996). Gravity wave activity in the upper mesosphere over Urbana, Illinois: Lidar observations and analysis of gravity wave propagation models. *Journal of Atmospheric and Solar-Terrestrial Physics*, *58*(16), 1905–1926. https://doi.org/10.1016/0021-9169(96)00026-8

Dewan, E. M., Picard, R. H., O'Neil, R. R., Gardiner, H. A., Gibson, J., Mill, J. D., et al. (1998). MSX satellite observations of thunderstorm-generated gravity waves in mid-wave infrared images of the upper stratosphere. *Geophysical Research Letters*, *25*(7), 939–942. https://doi.org/10.1029/98GL00640

Eckermann, S. D., Broutman, D., Ma, J., Doyle, J. D., Pautet, P.-D., Taylor, M. J., et al. (2016). Dynamics of orographic gravity waves observed in the mesosphere over Auckland Islands during the Deep Propagating Gravity Wave Experiment (DEEPWAVE). *Journal of the Atmospheric Sciences*, *73*(10), 3855–3876. https://doi.org/10.1175/JAS-D-16-0059.1

Eckermann, S. D., Ma, J., Hoppel, K. W., Kuhl, D. D., Allen, D. R., Doyle, J. A., et al. (2018). High-altitude (0–100 km) global atmospheric reanalysis system: Description and application to the 2014 austral winter of the Deep Propagating Gravity-Wave Experiment (DEEPWAVE). *Monthly Weather Review*, *146*(8), 2639–2666. https://doi.org/10.1175/MWR-D-17-0386.1

Eckermann, S. D., & Preusse, P. (1999). Global measurements of stratospheric mountain waves from space. *Science*, *286*(5444), 1534–1537. https://doi.org/10.1126/science.286.5444.1534

Fritts, D. C., & Alexander, M. J. (2003). Gravity wave dynamics and effects in the middle atmosphere. *Reviews of Geophysics*, *41*(1), 1003. https://doi.org/10.1029/2001RG000106

Fritts, D. C., Janches, D., & Hocking, W. K. (2010). Southern Argentina Agile Meteor Radar: Initial assessment of gravity wave momentum fluxes. *Journal of Geophysical Research*, *115*, D19123. https://doi.org/10.1029/2010JD013891

Fritts, D. C., & Lund, T. (2011). Gravity wave influences. In M. Abdu, & D. Pancheva (Eds.), *the thermosphere and ionosphere: Observations and recent modeling, Aeronomy of the Earth's atmosphere and ionosphere*, *IAGA Special Sopron Book Series* (Vol. 2). Dordrecht: Springer. https://doi.org/10.1007/978-94-007-0326-1_8

Fritts, D. C., Pautet, P.-D., Bossert, K., Taylor, M. J., Williams, B. P., Iimura, H., et al. (2014). Quantifying gravity wave momentum fluxes with mesosphere temperature mappers and correlative instrumentation. *Journal of Geophysical Research: Atmospheres*, *119*, 13,583–13,603. https://doi.org/10.1002/2014JD022150

Fritts, D. C., Smith, R. B., Taylor, M. J., Doyle, J. M., Eckermann, S. E., Dörnbrack, A., et al. (2016). The Deep Propagating Gravity Wave Experiment (DEEPWAVE): An airborne and ground-based exploration of gravity wave propagation and effects from their sources throughout the lower and middle atmosphere. *Bulletin of the American Meteorological Society*, *97*(3), 425–453. https://doi.org/10.1175/BAMS-D-14-00269.1

Fritts, D. C., Vosper, S. B., Williams, B. P., Bossert, K., Plane, J. M. C., Taylor, M. J., et al. (2018). Large-amplitude mountain waves accompanying weak cross-mountain flow during DEEPWAVE Research Flight RF22 on 13 July 2014. *Journal of Geophysical Research: Atmospheres*, *123*(18), 9992–10,022. https://doi.org/10.1029/2017JD028250

Garcia, F., Taylor, M. J., & Kelley, M. (1998). Two-dimensional spectral analysis of mesospheric airglow image data. *Applied Optics*, *36*, 7,374–7,385.

Garcia, R. R., & Solomon, S. (1985). The effects of breaking gravity waves on the dynamics and chemical composition of the mesosphere and lower thermosphere. *Journal of Geophysical Research*, *90*, 3850.

Gardner, C. S. (1991). Introduction to ALOHA-90: The airborne lidar and observations of the Hawaiian Airglow Campaign. *Geophysical Research Letters*, *18*(7), 1313–1316. https://doi.org/10.1029/91GL01294

Gardner, C. S. (1995). Introduction to ALOHA/ANLC-93: The 1993 airborne lidar and observations of the Hawaiian Airglow/Airborne Noctilucent Cloud Campaigns. *Geophysical Research Letters*, *22*(20), 2789–2792. https://doi.org/10.1029/95GL02782

Gardner, C. S. (2018). Role of wave induced diffusion and energy flux in the vertical transport of atmospheric constituents in the mesopause region. *Journal of Geophysical Research: Atmospheres*, *123*, 6581–6604. https://doi.org/10.1029/2018JD028359

Gardner, C. S., Gulati, K., Zhao, Y., & Swenson, G. (1999). Measuring gravity wave momentum fluxes with airglow imagers. *Journal of Geophysical Research*, *104*(D10), 11,903–11,915. https://doi.org/10.1029/1999JD900105

Gardner, C. S., Tao, X., & Papen, G. C. (1995). Simultaneous lidar observations of vertical wind, temperature, and density profiles in the upper mesosphere: Evidence for non separability of atmospheric perturbation spectra. *Geophysical Research Letters*, *22*(20), 2877–2880. https://doi.org/10.1029/95GL02783

Geller, M. A., Alexander, M. J., Love, P. T., Bacmeister, J., Ern, M., Hertzog, A., et al. (2013). A comparison between gravity wave momentum fluxes in observations and climate models. *Journal of Climate*, *26*(17), 6383–6405. https://doi.org/10.1175/JCLI-D-12-00545.1

Gisinger, S., Dörnbrack, A., Matthias, V., Doyle, J. D., Eckermann, S. D., Ehard, B., et al. (2017). Atmospheric conditions during the Deep Propagating Gravity Wave Experiment (DEEPWAVE). *Monthly Weather Review*, *145*(10), 4249–4275. https://doi.org/10.1175/MWR-D-16-0435.1

Heale, C. J., Bossert, K., Snively, J. B., Fritts, D. C., Pautet, P.-D., & Taylor, M. J. (2017). Numerical modeling of a multiscale gravity wave event and its airglow signatures over Mount Cook, New Zealand during the DEEPWAVE campaign. *Journal of Geophysical Research: Atmospheres*, *122*, 846–860. https://doi.org/10.1002/2016JD025700

Heale, C. J., Snively, J. B., & Hickey, M. P. (2014). Numerical simulation of the long-range propagation of gravity wave packets over Halley, Antarctica. *Journal of Geophysical Research: Atmospheres*, *119*, 11,116–11,134. https://doi.org/10.1002/2014JD022099

Hecht, J. H., Walterscheid, R. L., Fritts, D. C., Isler, J. R., Senft, D. C., Gardner, C. S., & Franke, S. J. (1997). Wave breaking signatures in OH airglow and sodium densities and temperatures. Part I: Airglow imaging, Na lidar, and MF radar observations. *Journal of Geophysical Research*, *102*(D6), 6655–6668. https://doi.org/10.1029/96JD02619

Hertzog, A., Alexander, M. J., & Plougonven, R. (2012). On the intermittency of gravity wave momentum flux in the stratosphere. *Journal of the Atmospheric Sciences*, *69*(11), 3433–3448. https://doi.org/10.1175/JAS-D-12-09.1

Hertzog, A., Boccara, G., Vincent, R. A., Vial, F., & Cocquerez, P. (2008). Estimation of gravity wave momentum flux and phase speeds from quasi-Lagrangian stratospheric balloon flights. Part II: Results from the Vorcore campaign in Antarctica. *Journal of the Atmospheric Sciences*, *65*(10), 3056–3070. https://doi.org/10.1175/2008JAS2710.1

Hoffmann, L., Xue, X., & Alexander, M. J. (2013). A global view of stratospheric gravity wave hotspots located with Atmospheric Infrared Sounder observations. *Journal of Geophysical Research: Atmospheres*, *118*, 416–434. https://doi.org/10.1029/2012JD018658

Holton, J. R. (1983). The influence of gravity wave breaking on the circulation of the middle atmosphere. *Journal of the Atmospheric Sciences*, *40*(10), 2497–2507. https://doi.org/10.1175/1520-0469(1983)040<2497:TIOGWB>2.0.CO;2

Jewtoukoff, V., Plougonven, R., & Hertzog, A. (2013). Gravity waves generated by deep tropical convection: Estimates from balloon observations and mesoscale simulations. *Journal of Geophysical Research: Atmospheres*, *118*, 9690–9707. https://doi.org/10.1002/jgrd.50781

Jiang, J. H., Wu, D. L., & Eckermann, S. D. (2002). Upper Atmosphere Research Satellite (UARS) MLS observation of mountain waves over the Andes. *Journal of Geophysical Research*, *107*(D20), 8273. https://doi.org/10.1029/2002JD002091

Kaifler, B., Kaifler, N., Ehard, B., Dörnbrack, A., Rapp, M., & Fritts, D. C. (2015). Influences of source conditions on mountain wave penetration into the stratosphere and mesosphere. *Geophysical Research Letters*, *42*, 9488–9494. https://doi.org/10.1002/2015GL066465

Kruse, C. G., Smith, R. B., & Eckermann, S. D. (2016). The midlatitude lower-stratospheric mountain wave valve layer. *Journal of the Atmospheric Sciences*, *73*(12), 5081–5100. https://doi.org/10.1175/JAS-D-16-0173.1

Li, Z., Liu, A. Z., Lu, X., Swenson, G. R., & Franke, S. J. (2011). Gravity wave characteristics from OH airglow imager over Maui. *Journal of Geophysical Research*, *116*, D22115. https://doi.org/10.1029/2011JD015870

Lindzen, R. S. (1981). Turbulence and stress owing to gravity wave and tidal breakdown. *Journal of Geophysical Research*, *86*(C10), 9707. https://doi.org/10.1029/JC086iC10p09707

Medeiros, A. F., Takahashi, H., Buriti, R. A., Fechine, J., Wrasse, C. M., & Gobbi, D. (2007). MLT gravity wave climatology in the South America equatorial region observed by airglow imager. *Annals of Geophysics*, *25*(2), 399–406. https://doi.org/10.5194/angeo-25-399-2007

Medeiros, A. F., Taylor, M. J., Takahashi, H., Batista, P. P., & Gobbi, D. (2003). An investigation of gravity wave activity in the low-latitude upper mesosphere: Propagation direction and wind filtering. *Journal of Geophysical Research*, *108*(D14), 4411. https://doi.org/10.1029/2002JD002593

Miller, S. D., Straka, W. C. III, Yue, J., Smith, S. M., Alexander, M. J., Hoffmann, L., et al. (2015). Upper atmospheric gravity wave details revealed in nightglow satellite imagery. *Proceedings of the National Academy of Sciences of the United States of America*, *112*(49), E6728–E6735. https://doi.org/10.1073/pnas.1508084112

Moreels, G., & Herse, M. (1977). Photographic evidence of waves around the 85 km level. *Planetary and Space Science*, *25*(3), 265–273. https://doi.org/10.1016/0032-0633(77)90137-4

Nakamura, T., Higashikawa, A., Tsuda, T., & Matsushita, Y. (1999). Seasonal variations of gravity wave structures in OH airglow with a CCD imager at Shigaraki. *Earth Planets Space*, *51*(7-8), 897–906. https://doi.org/10.1186/BF03353248

Nielsen, K., Taylor, M. J., Hibbins, R. E., & Jarvis, M. J. (2009). Climatology of short-period mesospheric gravity waves over Halley, Antarctica (76°S, 27°W). *Journal of Atmospheric and Solar-Terrestrial Physics*, *71*(8-9), 991–1000. https://doi.org/10.1016/j.jastp.2009.04.005

Nielsen, K., Taylor, M. J., Stockwell, R. G., & Jarvis, M. J. (2006). An unusual mesospheric bore event observed at high latitudes over Antarctica. *Geophysical Research Letters*, *33*, L07803. https://doi.org/10.1029/2005GL025649

Pautet, P.-D., Taylor, M. J., Fritts, D. C., Bossert, K., Williams, B. P., Broutman, D., et al. (2016). Large-amplitude mesospheric response to an orographic wave generated over the Southern Ocean Auckland Islands (50.7°S) during the DEEPWAVE project. *Journal of Geophysical Research: Atmospheres*, *121*, 1431–1441. https://doi.org/10.1002/2015JD024336

Pautet, P.-D., Taylor, M. J., Liu, A. Z., & Swenson, G. R. (2005). Climatology of short-period gravity waves observed over northern Australia during the Darwin Area Wave Experiment (DAWEX) and their dominant source regions. *Journal of Geophysical Research*, *110*, D03S90. https://doi.org/10.1029/2004JD004954

Pautet, P.-D., Taylor, M. J., Pendleton, W. R. Jr., Zhao, Y., Yuan, T., Esplin, R., & McLain, D. (2014). An Advanced Mesospheric Temperature Mapper for high-latitude airglow studies. *Applied Optics*, *53*(26), 5934–5943.

Pautet, P.-D., Taylor, M. J., Snively, J. B., & Solorio, C. (2018). Unexpected occurrence of mesospheric frontal gravity wave events over South Pole (90°S). *Journal of Geophysical Research: Atmospheres*, *123*, 160–173. https://doi.org/10.1002/2017JD027046

Perwitasari, S., Sakanoi, T., Nakamura, T., Ejiri, M. K., Tsutsumi, M., Tomikawa, Y., et al. (2016). Three years of concentric gravity wave variability in the mesopause as observed by IMAP/VISI. *Geophysical Research Letters*, *43*, 11,528–11,535. https://doi.org/10.1002/2016GL071511

Plougonven, R., Hertzog, A., & Guez, L. (2013). Gravity waves over Antarctica and the Southern Ocean: Consistent momentum fluxes in mesoscale simulations and stratospheric balloon observations. *Quarterly Journal of the Royal Meteorological Society*, *139*(670), 101–118. https://doi.org/10.1002/qj.1965

Portele, T., Dörnbrack, A., Wagner, J., Gisinger, S., Ehard, B., Pautet, P., & Rapp, M. (2018). Mountain wave propagation under transient tropospheric forcing: A DEEPWAVE case study. *Monthly Weather Review*, *146*(6), 1861–1888. https://doi.org/10.1175/MWR-D-17-0080.1

Preusse, P., Ern, M., Bechtold, P., Eckermann, S. D., Kalisch, S., Trinh, Q. T., & Riese, M. (2014). Characteristics of gravity waves resolved by ECMWF. *Atmospheric Chemistry and Physics*, *14*(19), 10483–10508. https://doi.org/10.5194/acp-14-10483-2014

Qian, L., Solomon, S. C., & Kane, T. J. (2009). Seasonal variation of thermospheric density and composition. *Journal of Geophysical Research*, *114*, A01312. https://doi.org/10.1029/2008JA013643

Reid, I. M., & Vincent, R. A. (1987). Measurements of mesospheric gravity wave momentum fluxes and mean flow accelerations at Adelaide, Australia. *Journal of Atmospheric and Solar-Terrestrial Physics*, *49*(5), 443–460. https://doi.org/10.1016/0021-9169(87)90039-0

Ribstein, B., & Achatz, U. (2016). The interaction between gravity waves and solar tides in a linear tidal model with a 4-D ray-tracing gravity-wave parameterization. *Journal of Geophysical Research: Space Physics*, *121*, 8936–8950. https://doi.org/10.1002/2016JA022478

Salinas, C. C. J. H., Chang, L. C., Liang, M.-C., Yue, J., Russell, J. III, & Mlynczak, M. (2016). Impacts of SABER CO_2-based eddy diffusion coefficients in the lower thermosphere on the ionosphere/thermosphere. *Journal of Geophysical Research: Space Physics*, *121*, 12,080–12,092. https://doi.org/10.1002/2016JA023161

Senft, D. C., & Gardner, C. S. (1991). Seasonal variability of gravity wave activity and spectra in the mesopause region at Urbana. *Journal of Geophysical Research*, *96*(D9), 17229–17,264. https://doi.org/10.1029/91JD01662

Shutts, G. J., & Vosper, S. B. (2011). Stratospheric gravity waves revealed in NWP model forecasts. *Quarterly Journal of the Royal Meteorological Society*, *137*(655), 303–317. https://doi.org/10.1002/qj.763

Snively, J. B., & Pasko, V. P. (2005). Antiphase OH and OI airglow emissions induced by a short-period ducted gravity wave. *Geophysical Research Letters*, *32*, L08808. https://doi.org/10.1029/2004GL022221

Taylor, M. J., Pendleton, W. R., Clark, S., Takahashi, H., Gobbi, D., & Goldberg, R. A. (1997). Image measurements of short-period gravity waves at equatorial latitudes. *Journal of Geophysical Research*, *102*(D22), 26283–26299. https://doi.org/10.1029/96JD03515

Tsuda, T., Murayama, Y., Yamamoto, M., Kato, S., & Fukao, S. (1990). Seasonal variation of momentum flux in the mesosphere observed with the MU radar. *Geophysical Research Letters*, *17*(6), 725–728. https://doi.org/10.1029/GL017i006p00725

Vosper, S. B. (2015). Mountain waves and wakes generated by South Georgia: Implications for drag parametrization. *Quarterly Journal of the Royal Meteorological Society*, *141*(692), 2813–2827. https://doi.org/10.1002/qj.2566

Walterscheid, R. L., Hecht, J. H., Vincent, R. A., Reid, I. M., Woithe, J., & Hickey, M. P. (1999). Analysis and interpretation of airglow and radar observations of quasi-monochromatic gravity waves in the upper mesosphere and lower thermosphere over Adelaide, Australia (35 S, 138 E). *Journal of Atmospheric and Solar-Terrestrial Physics*, *61*(6), 461–478. https://doi.org/10.1016/S1364-6826(99)00002-4

Williams, B. P., Fritts, D. C., She, C.-Y., & Goldberg, R. A. (2006). Gravity wave propagation through a large semidiurnal tide and instabilities in the mesosphere and lower thermosphere during the winter 2003 MaCWAVE rocket campaign. *Annals of Geophysics*, *24*(4), 1199–1208. https://doi.org/10.5194/angeo-24-1199-2006

Wright, C. J., Osprey, S. M., & Gille, J. C. (2013). Global observations of gravity wave intermittency and its impact on the observed momentum flux morphology. *Journal of Geophysical Research: Atmospheres*, *118*, 10,980–10,993. https://doi.org/10.1002/jgrd.50869

Wu, D. L., Preusse, P., Eckermann, S. D., Jiang, J. H., de la Torre Juarez, M., Coy, L., & Wang, D. Y. (2006). Remote sounding of atmospheric gravitywaves with satellite limb and nadir techniques. *Advances in Space Research*, *37*, 2269–2277.

Wu, D. L., & Waters, J. W. (1996). Satellite observations of atmospheric variances: A possible indication of gravity waves. *Geophysical Research Letters*, *23*(24), 3631–3634. https://doi.org/10.1029/96GL02907

Yiğit, E., & Medvedev, A. S. (2010). Internal gravity waves in the thermosphere during low and high solar activity: Simulation study. *Journal of Geophysical Research*, *115*, A00G02. https://doi.org/10.1029/2009JA015106

Yiğit, E., & Medvedev, A. S. (2015). Internal wave coupling processes in Earth's atmosphere. *Advances in Space Research*, *55*(4), 983–1003. https://doi.org/10.1016/j.asr.2014.11.020

Yue, J., Miller, S. D., Hoffmann, L., & Straka, W. C. III (2014). Stratospheric and mesospheric concentric gravity waves over Tropical Cyclone Mahasen: Joint AIRS and VIIRS satellite observations. *Journal of Atmospheric and Solar-Terrestrial Physics*, *119*, 83–90. https://doi.org/10.1016/j.jastp.2014.07.003